Advancing Atmospheric River Forecasts into Subseasonal-to-Seasonal Timescales

Cory F. Baggett[1], Elizabeth A. Barnes[1], Eric D. Maloney[1], and Bryan D. Mundhenk[1]

[1]Department of Atmospheric Science, Colorado State University, Fort Collins, CO, USA

Corresponding author: Cory Baggett (cbaggett@rams.colostate.edu)

Key Points:

- The potential exists to forecast atmospheric river (AR) activity at subseasonal-to-seasonal (S2S) lead times of 3-5 weeks.
- Strong MJO and QBO activity modulates AR activity at S2S lead times.
- Numerical weather models predict AR activity with positive skill scores that vary with the MJO and QBO but lack skill at S2S lead times.

Abstract

Atmospheric rivers are elongated plumes of intense moisture transport that are capable of producing extreme and impactful weather. Along the west coast of North America, they occasionally cause considerable mayhem – delivering flooding rains during periods of heightened activity and desiccating droughts during periods of reduced activity. The intrinsic chaos of the atmosphere makes the prediction of atmospheric rivers at subseasonal-to-seasonal timescales (3 to 5 weeks) an inherently difficult task. We demonstrate here that the potential exists to advance forecast lead times of atmospheric rivers into subseasonal-to-seasonal timescales through knowledge of two of the atmosphere's most prominent oscillations, the Madden-Julian oscillation (MJO) and the quasi-biennial oscillation (QBO). Strong MJO and QBO activity modulates the frequency at which atmospheric rivers strike – offering an opportunity to improve subseasonal-to-seasonal forecast models and thereby skillfully predict atmospheric river activity up to 5 weeks in advance.

1 Introduction

During the winter of 2016-17, atmospheric rivers (ARs; Text S1) [*Ralph and Dettinger*, 2011; *Gimeno et al.*, 2014] repeatedly struck the U.S. West Coast delivering copious amounts of precipitation that replenished reservoirs and snowpacks that had been decimated by a relentless, unprecedented drought during the previous several years [*Griffin and Anchukaitis*, 2014]. Because of their profound societal impacts, ARs striking the West Coast have garnered significant interest from policymakers and extensive research by scientists [e.g, *Zhu and Newell*, 1998; *Ralph et al.*, 2004; *Ralph and Dettinger*, 2011; *Guan et al.*, 2012; *Gimeno et al.*, 2014; *Griffin and Anchukaitis*, 2014; *Payne and Magnusdottir*, 2014; *Guan and Waliser*, 2015; *Mundhenk et al.*, 2016a; *Mundhenk et al.*, 2016b; *Waliser and Guan*, 2017]. Meanwhile, increasing scrutiny has also been given to the climatic impact of ARs at higher latitudes, particularly those that strike Alaska and cause flooding [*Mundhenk et al.*, 2016b] or those that penetrate into the Arctic where they can cause warming and sea-ice loss [*Doyle et al.*, 2011; *Liu and Barnes*, 2015; *Baggett et al.*, 2016; *Woods and Caballero*, 2016]. Since their impacts are so extreme, it would be beneficial to have as much forewarning as possible to prepare for periods of heightened or suppressed AR activity. While numerical weather models successfully predict ARs with forecast lead times of ~10 to 14 days [*Wick et al.*, 2013], this is often insufficient time for officials to adequately prepare. For example, in preparation for heightened AR activity, hydrologists could use forecasts with lead times that extend into sub-seasonal-to-seasonal (S2S) timescales (3 to 5 weeks) to safely drawdown the water level of reservoirs. However, if a reservoir, such as Lake Oroville in California, has to be drawn down hastily – such as was the case this past winter – there are inherent risks. On 11 February 2017, in anticipation of imminent AR activity, the emergency spillway of Lake Oroville's dam was used to reduce the load on its

heavily eroded, main spillway. However, the emergency spillway itself also experienced dangerous erosion and threatened to fail, prompting the mass evacuation of inhabitants living downstream. Fortunately, a catastrophic failure did not occur and emergency officials averted disaster.

Our results show the potential to extend lead times of skillful AR forecasts beyond the ~10 to 14 day predictability barrier into S2S timescales. We accomplish this by harnessing knowledge of the current state of two of the atmosphere's most prominent oscillations: the Madden-Julian oscillation (MJO) [*Madden and Julian*, 1994; *Waliser et al.*, 2003; *Kiladis et al.*, 2014] and the stratospheric quasi-biennial oscillation (QBO) [*Baldwin et al.*, 2001]. The MJO consists of anomalous tropical convection and zonal winds that propagate eastward along the equator with a period of ~30 to 90 days. These tropical convective anomalies induce Rossby wave trains that propagate poleward, influencing the weather in the mid-latitudes at distant locations [*Hoskins and Karoly*, 1981; *Sardeshmukh and Hoskins*, 1988; *Matthews et al.*, 2004; *Seo and Son*, 2012; *Zhang*, 2013; *Baggett et al.*, 2016; *Henderson et al.*, 2016]. In particular, the phase of the MJO [*Wheeler and Hendon*, 2004; *Kiladis et al.*, 2014] modulates both the frequency of occurrence and the location of AR strikes along the west coast of North America [*Guan et al.*, 2012; *Guan and Waliser*, 2015; *Baggett et al.*, 2016; *Mundhenk et al.*, 2016a]. The QBO is a quite different oscillation. It consists of zonal wind anomalies in the tropical stratosphere (~15 km above the surface) that propagate downward, cycling between easterly and westerly phases with a period of ~2 to 3 years. These stratospheric anomalies are capable of modulating tropical convective anomalies in the troposphere [*Yoo and Son*, 2016]. In fact, it was recently demonstrated that the QBO can modulate the amplitude of the MJO [*Yoo and Son*, 2016; *Hood*, 2017; *Son et al.*, 2017]. Moreover, depending on the phase of the QBO, numerical

weather models have varying skill in predicting the MJO at S2S timescales [*Marshall et al.*, 2016].

Despite our emerging understanding of the QBO's influence on the MJO, little research has been conducted on their combined influence on the weather in the mid-latitudes [*Liu et al.*, 2014; *Son et al.*, 2017]. Here, we present evidence derived from the European Centre for Medium-Range Weather Forecasts (ECMWF) interim reanalysis (ERA-Interim) dataset [*Dee et al.*, 2011] that the phase of the QBO modulates the frequency and the location of AR strikes associated with the MJO. This modulation is observable with lead times of 3 to 5 weeks, extending well into S2S timescales. Moreover, we demonstrate that the state-of-the-art ECMWF reforecast ensemble system [*Vitart et al.*, 2017] forecasts AR strikes with positive skill scores at lead times that only extend to approximately two weeks. We find that these skill scores vary according to the current state of both the MJO and the QBO.

2 Subseasonal modulation of AR activity by the MJO and QBO

Throughout this study, we employ the outgoing-longwave radiation-based MJO index (OMI; Text S2) [*Kiladis et al.*, 2014] and a QBO index (Text S3) identical to that defined by *Yoo and Son* (2016). We confine our analysis to November through February, when ARs are the most active along the west coast of North America [*Guan and Waliser*, 2015; *Mundhenk et al.*, 2016a]. We identify ARs in the ERA-Interim dataset, from which we have acquired instantaneous (0000 UTC) daily values of zonal wind u, meridional wind v, specific humidity q, and geopotential. The data we download has a horizontal resolution of 1.5° by 1.5° and a vertical resolution of 10 pressure levels, spanning from 1979-2015. The chosen resolution matches that of the ECMWF reforecast ensemble system. We employ a detection algorithm [*Mundhenk et al.*, 2016a; *Mundhenk et al.*, 2016b] that searches for coherent, horizontal regions of highly

anomalous, vertically integrated vapor transport (IVT; Text S4) that satisfy certain geometric criteria typical of an AR. We provide further details of the AR detection algorithm in Text S5. Two such ARs that exemplify the results of the detection algorithm are depicted (black vectors) striking the Pacific Northwest in Figure 1a and Alaska in Figure 1b. While we primarily focus on the Pacific Northwest and Alaska regions, results for California and an expanded Pacific Northwest which includes Northern California are provided in Figures S1-S4.

The locations where the ARs strike in Figure 1 depend largely on the configuration of the large-scale atmospheric circulation as depicted by the 500-hPa geopotential height anomalies (color shading). The strike on the Pacific Northwest occurs when negative height anomalies are present in the Gulf of Alaska, whereas opposite signed anomalies are observed during the strike on Alaska [*Mundhenk et al.*, 2016b]. It is noteworthy that both of these ARs occurred during the third week following the propagation of the MJO through phase 5 over the Maritime Continent region. The disparity of these strike locations suggests that knowledge of the MJO alone may not be sufficient for predicting AR strikes at extended lead times. Indeed, these particular strikes on the Pacific Northwest and Alaska occurred during the easterly and westerly phases of the QBO, respectively, alluding to the possibility that the phase of the QBO may at least partially explain their disparate strike locations.

To test this hypothesis, Figures 2b and 2c depict 500-hPa geopotential height anomalies and anomalous IVT associated with ARs ($IVT_{AR;}$ Text S6), composited over the third week following days when the MJO was in phase 5 during easterly and westerly QBO phases, respectively. When segregated by QBO phase, the geopotential height anomalies appear vastly different than the composite of events made independent of the phase of the QBO (Figure 2a). Most notably, and similar to the two individual events displayed in Figure 1, negative height

anomalies exist in the Gulf of Alaska for the composite of easterly QBO periods (Figure 2b), whereas positive height anomalies are present during westerly QBO periods (Figure 2c). Because of the configuration of these height anomalies, anomalous IVT_{AR} points away from Alaska (indicating a reduction in AR strikes) and toward the Pacific Northwest (indicating an increase in AR strikes) during the easterly QBO, and vice versa during the westerly QBO. It is important to emphasize that the composites in Figure 2 only illustrate the third week following days when the MJO was in phase 5. In Figure S6 we depict the difference between the easterly QBO and the westerly QBO composites out to 5 weeks following all 8 phases of the MJO. More often than not, these weekly composites illustrate significant differences between their easterly and westerly QBO counterparts (e.g., Figure 2d). These plots suggest that knowledge of the current states of both the MJO and the QBO is much more useful for forecasting AR strikes at extended lead times than knowledge of the MJO alone [*Guan and Waliser*, 2015; *Mundhenk et al.*, 2016a].

In Figure 3, we illustrate how AR strikes per week on the Pacific Northwest and Alaska are modulated by the combined effects of the MJO and QBO at extended lead times out to five weeks. The detection grid points used to count AR strikes for the Pacific Northwest and Alaska are shown (green squares) in Figures 1a and 1b, respectively. If an AR intersects any of the detection grid points, we consider a strike to have occurred on that region on that day. For each day in our observational dataset, we count the number of AR strikes that occur over the course of the following week (integers ranging from 0 to 7 because our dataset has a daily temporal resolution) and subtract its calendar day climatological value to determine that day's anomalous AR strikes per week. We then make composites of this value as a function of the phase of the MJO, the phase of the QBO, and lead time. Although it is possible that the same AR may impact a region over consecutive days, our goal is to detect heightened AR activity rather than simply

count unique ARs. Furthermore, by counting AR strikes over a given week, we reduce the noisiness of the synoptic-scale variability associated with ARs, particularly at S2S timescales.

The first column of Figure 3 depicts anomalous AR activity over the Pacific Northwest. During easterly QBO periods (Figure 3a), anomalously high AR activity shows an extraordinarily steady propagation across lead time and MJO phase. We observe high activity during the fifth week following phase 3 of the MJO that transitions steadily to the first and second weeks following phases 6 and 7. Also, consistent with Figure 2b, we observe high AR activity during the third week following phase 5 (black square in Figure 3a). During westerly QBO periods (Figure 3b), anomalous AR activity again shows a remarkably steady propagation across lead time and MJO phase. However, the anomalies during westerly QBO periods are nearly everywhere opposite to those during easterly QBO periods. For example, consistent with Figure 2c, we observe low AR activity over the Pacific Northwest during the third week following phase 5 (black square Figure 3b). Indeed, because of their complementarity, a composite independent of the phase of the QBO (Figure S4) reveals greatly diminished anomalies compared to those in Figures 3a and 3b. Turning to Alaska (second column of Figure 3), the composites based on easterly and westerly QBO periods do not exhibit the same complementarity as they do for the Pacific Northwest, although they do differ. In general, AR strikes on Alaska display a clearer propagating signal and are favored during westerly QBO periods (compare Figures 3c and 3d), particularly during the second and third weeks following phase 5 of the MJO (consistent with Figure 2c). To conclude our discussion of Figure 3, we underscore that there is a clear, observable modulation of AR activity at lead times of 3 to 5 weeks. This modulation becomes apparent when both the phases of the MJO and the QBO are

considered, and it has the potential to advance our skillful forecasting of AR activity into S2S timescales.

3 The predictive skill of AR activity by the ECMWF model

Given the potential predictability of anomalous AR activity on display at extended lead times in Figure 3, we now desire to see if state-of-the-art numerical weather models can skillfully predict AR activity at S2S timescales. Moreover, we wish to see if this skill varies as a function of the phases of the MJO and QBO. To this end, we use reforecasts from the ECMWF reforecast ensemble system (consisting of 1 control and 10 perturbed members), acquired from the World Weather Research Program/World Climate Research Program (WWRP/WWCR) S2S Prediction Project database [*Vitart et al.*, 2017]. Further details on the model may be found in Text S7. To assess the reforecast model's ability to predict observed AR activity, we calculate its Logarithmic Skill Score (LSS; Text S8) [*Tippett et al.*, 2017]. In general, the LSS is useful in an ensemble framework because it is capable of scoring probabilistic forecasts of various categories of outcomes. In our situation, these categories correspond to the number of predicted AR strikes per week (integers ranging from 0 to 7 because the model output has a daily temporal resolution) with each category assigned a probability based on the number of ensembles that predict it. The ensemble forecast is then graded by comparing how well it forecasted the actual observed outcome versus a reference forecast based solely on the climatological number of AR strikes per week.

Figure 4 displays the LSSs for the ECMWF reforecast ensemble system's prediction of AR strikes on the Pacific Northwest and Alaska. In general, positive skill scores exist at short lead times but do not extend beyond 14 days into S2S timescales (Figures 4a, 4b, 4d and 4e). In fact, at S2S timescales, the model primarily has negative skill scores that imply a climatological

forecast of AR activity may be more skillful than the model's. The reason for the decline in skill scores at S2S timescales is beyond the scope of this current study, but it could be due to a bias in the mean-state of the model or simply due to the ~10-14 day predictability barrier that currently exists in forecasting the mid-latitude ARs [*Wick et al.*, 2013]. Regardless, when examining the skill scores as a function of MJO and QBO phase, there are notable differences. In both regions, the model shows greater relative skill during phases 7, 8, and 1 of the MJO during easterly QBO periods as opposed to westerly QBO periods (Figures 4c and 4f). In contrast, the model has more skill during westerly QBO periods when the MJO is in phases 3, 4, and 5 (Figures 4c and 4f). Therefore, the model's ability to skillfully forecast the observed modulation of AR activity by the MJO and QBO (Figure 3) varies itself according to the MJO and QBO. In practice, if the model is predicting enhanced AR activity over Alaska during the second week following phase 5 of the MJO, then a discerning forecaster may be reasonably confident in the accuracy of this forecast if the QBO is westerly (Figures 3d and 4f).

4 Advancing predictive skill into subseasonal timescales

A few interesting questions arise naturally from the results of this study. First, what are the physical mechanisms by which the QBO modulates the MJO and its impact on the weather in the mid-latitudes? Secondly, to what extent does the ECMWF reforecast ensemble system and other S2S models accurately simulate them? To address the first question, there is emerging evidence that the QBO's influence on the MJO derives from its ability to reduce or enhance the static stability in the upper troposphere/lower stratosphere region. In the case of reduced static stability associated with the easterly QBO, one would expect enhanced convection and a higher amplitude MJO [*Yoo and Son*, 2016; *Hood*, 2017]. Moreover, this modulation occurs in a manner independent of the tropics most dominant interannual mode of variability, the El-Niño-Southern

Oscillation (ENSO; Text S9) [*Nie and Sobel*, 2015; *Yoo and Son*, 2016; *Son et al.*, 2017]. However, how and to what extent this modulation impacts the weather in the mid-latitudes is not well understood and is likely dependent on mid-latitude variability itself [*Sardeshmukh and Hoskins*, 1988; *Henderson et al.*, 2017].

With respect to the ECMWF reforecast ensemble system's ability to simulate the physical mechanisms observed in the atmosphere, recent work has shown that S2S models are becoming more skillful in predicting the MJO with lead times approaching 3 to 4 weeks [*Kim et al.*, 2016; *Marshall et al.*, 2016; *Green et al.*, 2017; *Vitart*, 2017]. Moreover, their skill scores are dependent on the phase of the QBO [*Marshall et al.*, 2016]. However, here we show that the ECMWF reforecast ensemble system has little skill in predicting ARs in the mid-latitudes beyond lead times of 2 weeks (Figure 4). Thus, it is critical to understand this disparity in skill scores – whether it derives from inaccurate simulations of the QBO, biases in the physical mechanisms linking the tropics to the mid-latitudes, or some other reason. Nonetheless, our observational results show evidence that ARs have the potential to be forecasted more accurately at lead times of 3 to 5 weeks when the phases of both the MJO and the QBO are considered. Lead times of this length push the envelope of AR predictability into S2S timescales, offering a significant advance in forewarning for ARs and their extreme impacts.

Acknowledgments

This research was supported by NOAA's Modeling, Analysis, Predictions, and Projections (MAPP) Program grant NA16OAR4310064 and NSF's Climate and Large-scale Dynamics Program grant AGS-1441916. We thank Kyle Nardi and Kai-Chih Tseng for their assistance in acquiring the data and Michelle L'Heureux for her help in calculating the LSS. All coding was performed in Python V2.7.8 and in the National Center for Atmospheric Research

238 Command Language (NCL) version V6.4.0. Data repositories and are provided in Text S10.

239 Access information to the AR detection algorithm are provided in Text S5.

240 **References**

241 Baggett, C., S. Lee, and S. Feldstein (2016), An investigation of the presence of atmospheric
242 rivers over the North Pacific during planetary-scale wave life cycles and their role in
243 Arctic warming, J. Atmos. Sci., 73(11), 4329-4347, doi:10.1175/JAS-D-16-0033.1.

244 Baldwin, M. P., et al. (2001), The quasi-biennial oscillation, Rev. Geophys., 39(2), 179-229,
245 doi:10.1029/1999RG000073.

246 Dee, D. P., et al. (2011), The ERA-Interim reanalysis: configuration and performance of the data
247 assimilation system, Q. J. Roy. Meteor. Soc., 137(656), 553-597, doi:10.1002/QJ.828.

248 Dettinger, M. D., F. M. Ralph, T. Das, P. J. Neiman, and D. R. Cayan (2011), Atmospheric
249 Rivers, Floods and the Water Resources of California, Water-Sui, 3(2), 445-478,
250 doi:10.3390/W3020445.

251 Doyle, J. G., G. Lesins, C. P. Thackray, C. Perro, G. J. Nott, T. J. Duck, R. Damoah, and J. R.
252 Drummond (2011), Water vapor intrusions into the High Arctic during winter, Geophys.
253 Res. Lett., 38, doi:10.1029/2011GL047493.

254 Gimeno, L., R. Nieto, M. Vázquez, and D. Lavers (2014), Atmospheric rivers: a mini-review
255 Frontiers in Earth Science, 2, 1-6, doi:10.3389/FEART.2014.00002.

256 Green, B. W., S. Sun, R. Bleck, S. G. Benjamin, and G. A. Grell (2017), Evaluation of MJO
257 predictive skill in multi-physics and multi-model global ensembles, Mon. Weather Rev.,
258 in press, doi:10.1175/MWR-D-16-0419.1.

259 Griffin, D., and K. J. Anchukaitis (2014), How unusual is the 2012-2014 California drought?,
260 Geophys. Res. Lett., 41(24), 9017-9023, doi:10.1002/2014GL062433.

261 Guan, B., and D. E. Waliser (2015), Detection of atmospheric rivers: Evaluation and application
262 of an algorithm for global studies, J. Geophys. Res.-Atmos., 120(24), 12514-12535, doi:
263 10.1002/2015JD024257.

264 Guan, B., D. E. Waliser, N. P. Molotch, E. J. Fetzer, and P. J. Neiman (2012), Does the Madden-
265 Julian oscillation influence wintertime atmospheric rivers and snowpack in the Sierra
266 Nevada?, Mon. Weather Rev., 140(2), 325-342, doi:10.1175/MWR-D-11-00087.1.

267 Henderson, S. A., E. D. Maloney, and E. A. Barnes (2016), The Influence of the Madden-Julian
268 oscillation on Northern Hemisphere winter blocking, J. Climate, 29(12), 4597-4616,
269 doi:10.1175/JCLI-D-15-0502.1.

270 Henderson, S. A., E. D. Maloney, and S. W. Son (2017), Madden-Julian oscillation Pacific
271 teleconnections: The impact of the basic state and MJO representation in general
272 circulation models, J. Climate, in press, doi:10.1175/JCLI-D-16-0789.1.

273 Hood, L. L. (2017), QBO/Solar modulation of the boreal winter Madden-Julian oscillation: A
274 prediction for the coming solar minimum, Geophys. Res. Lett., in press,
275 doi:10.1002/2017GL072832.

276 Hoskins, B. J., and D. J. Karoly (1981), The steady linear response of a spherical atmosphere to
277 thermal and orographic forcing, J. Atmos. Sci., 38(6), 1179-1196.

278 Kiladis, G. N., J. Dias, K. H. Straub, M. C. Wheeler, S. N. Tulich, K. Kikuchi, K. M.
279 Weickmann, and M. J. Ventrice (2014), A comparison of OLR and circulation-based
280 indices for tracking the MJO, Mon. Weather Rev., 142(5), 1697-1715,
281 doi:10.1175/MWR-D-13-00301.1.

Kim, H. M., D. Kim, F. Vitart, V. E. Toma, J. S. Kug, and P. J. Webster (2016), MJO propagation across the Maritime Continent in the ECMWF Ensemble Prediction System, J. Climate, 29(11), 3973-3988, doi:10.1175/JCLI-D-15-0862.1.

Liu, C. J., and E. A. Barnes (2015), Extreme moisture transport into the Arctic linked to Rossby wave breaking, J. Geophys. Res.-Atmos., 120(9), 3774-3788, doi:10.1002/2014JD022796.

Liu, C. X., B. J. Tian, K. F. Li, G. L. Manney, N. J. Livesey, Y. L. Yung, and D. E. Waliser (2014), Northern Hemisphere mid-winter vortex-displacement and vortex-split stratospheric sudden warmings: Influence of the Madden-Julian oscillation and quasi-Biennial oscillation, J. Geophys. Res.-Atmos., 119(22), 12599-12620, doi:10.1002/2014JD021876.

Madden, R. A., and P. R. Julian (1994), Observations of the 40-50-Day tropical oscillation - a Review, Mon. Weather Rev., 122(5), 814-837.

Marshall, A. G., H. H. Hendon, S. W. Son, and Y. Lim (2016), Impact of the Quasi-Biennial oscillation on predictability of the Madden–Julian oscillation, Climate Dynamics, in press, doi:10.1007/S00382-016-3392-0.

Matthews, A. J., B. J. Hoskins, and M. Masutani (2004), The global response to tropical heating in the Madden-Julian oscillation during the northern winter, Q. J. Roy. Meteor. Soc., 130(601), 1991-2011, doi:10.1256/QJ.02.123.

Mundhenk, B. D., E. A. Barnes, and E. D. Maloney (2016a), All-season climatology and variability of atmospheric river frequencies over the North Pacific, J. Climate, 29(13), 4885-4903, doi:10.1175/JCLI-D-15-0655.1.

304 Mundhenk, B. D., E. A. Barnes, E. D. Maloney, and K. M. Nardi (2016b), Modulation of
305 atmospheric rivers near Alaska and the US West Coast by northeast Pacific height
306 anomalies, J. Geophys. Res.-Atmos., 121(21), 12751-12765, doi:10.1002/2016JD025350.

307 Nie, J., and A. H. Sobel (2015), Responses of tropical deep convection to the QBO: Cloud-
308 resolving simulations, J. Atmos. Sci., 72(9), 3625-3638, doi:10.1175/JAS-D-15-0035.1.

309 Payne, A. E., and G. Magnusdottir (2014), Dynamics of landfalling atmospheric rivers over the
310 North Pacific in 30 Years of MERRA Reanalysis, J. Climate, 27(18), 7133-7150,
311 doi:10.1175/JCLI-D-14-00034.1.

312 Ralph, F. M., and M. D. Dettinger (2011), Storms, floods, and the science of atmospheric rivers,
313 EOS, Transactions American Geophysical Union, 92(32), 265-266,
314 doi:10.1029/2011EO320001.

315 Ralph, F. M., P. J. Neiman, and G. A. Wick (2004), Satellite and CALJET aircraft observations
316 of atmospheric rivers over the eastern north pacific ocean during the winter of 1997/98,
317 Mon. Weather Rev., 132(7), 1721-1745.

318 Roulston, M. S., and L. A. Smith (2002), Evaluating probabilistic forecasts using information
319 theory, Mon. Weather Rev., 130(6), 1653-1660.

320 Sardeshmukh, P. D., and B. J. Hoskins (1988), The generation of global rotational flow by steady
321 idealized tropical divergence, J. Atmos. Sci., 45(7), 1228-1251.

322 Seo, K. H., and S. W. Son (2012), The global atmospheric circulation response to tropical
323 diabatic heating associated with the Madden-Julian oscillation during northern Winter, J.
324 Atmos. Sci., 69(1), 79-96, doi:10.1175/2011JAS3686.1.

Sodemann, H., and A. Stohl (2013), Moisture origin and meridional transport in atmospheric rivers and their association with multiple cyclones, Mon. Weather Rev., 141(8), 2850-2868, doi:10.1175/MWR-D-12-00256.1.

Son, S. W., Y. Lim, C. H. Yoo, H. H. Hendon, and J. Kim (2017), Stratospheric control of the Madden-Julian oscillation, J. Climate, 30(6), 1909-1922, doi:10.1175/JCLI-D-16-0620.1.

Tippett, M. K., M. Ranganathan, M. L'Heureux, A. G. Barnston, and T. DelSole (2017), Assessing probabilistic predictions of ENSO phase and intensity from the North American Multimodel Ensemble, Climate Dynamics, in press, doi:10.1007/S00382-017-3721-Y.

Vitart, F., et al. (2017), The subseasonal to seasonal (S2S) prediction project database, Bulletin of the American Meteorological Society, 98(1), 163-173, doi:10.1175/BAMS-D-16-0017.1.

Vitart, F. (2017), Madden-Julian oscillation prediction and teleconnections in the S2S database, in press, doi:10.1002/QJ.3079.

Waliser, D., and B. Guan (2017), Extreme winds and precipitation during landfall of atmospheric rivers, Nat. Geosci., 10(3), 179-183, doi:10.1038/NGEO2894.

Waliser, D. E., K. M. Lau, W. Stern, and C. Jones (2003), Potential predictability of the Madden-Julian oscillation, Bulletin of the American Meteorological Society, 84(1), 33-50, doi:10.1175/BAMS-84-1-33.

Wheeler, M. C., and H. H. Hendon (2004), An all-season real-time multivariate MJO index: Development of an index for monitoring and prediction, Mon. Weather Rev., 132(8), 1917-1932.

Wick, G. A., P. J. Neiman, F. M. Ralph, and T. M. Hamill (2013), Evaluation of forecasts of the water vapor signature of atmospheric rivers in operational numerical weather prediction models, Weather Forecast, 28(6), 1337-1352, doi:10.1175/WAF-D-13-00025.1.

Wilks, D. S. (2011), Statistical methods in the atmospheric sciences, 2 ed., Academic Press, U.S.A.

Woods, C., and R. Caballero (2016), The role of moist intrusions in winter Arctic warming and wea ice decline, J. Climate, 29(12), 4473-4485, doi:10.1175/JCLI-D-15-0773.1.

Yoo, C., and S. W. Son (2016), Modulation of the boreal wintertime Madden-Julian oscillation by the stratospheric quasi-biennial oscillation, Geophys. Res. Lett., 43(3), 1392-1398, doi:10.1002/2016GL067762.

Zhang, C. (2013), Madden–Julian oscillation: Bridging weather and climate, Bulletin of the American Meteorological Society, 94(12), 1849-1870, doi:10.1175/BAMS-D-12-00026.1.

Zhu, Y., and R. E. Newell (1998), A proposed algorithm for moisture fluxes from atmospheric rivers, Mon. Weather Rev., 126(3), 725-735.

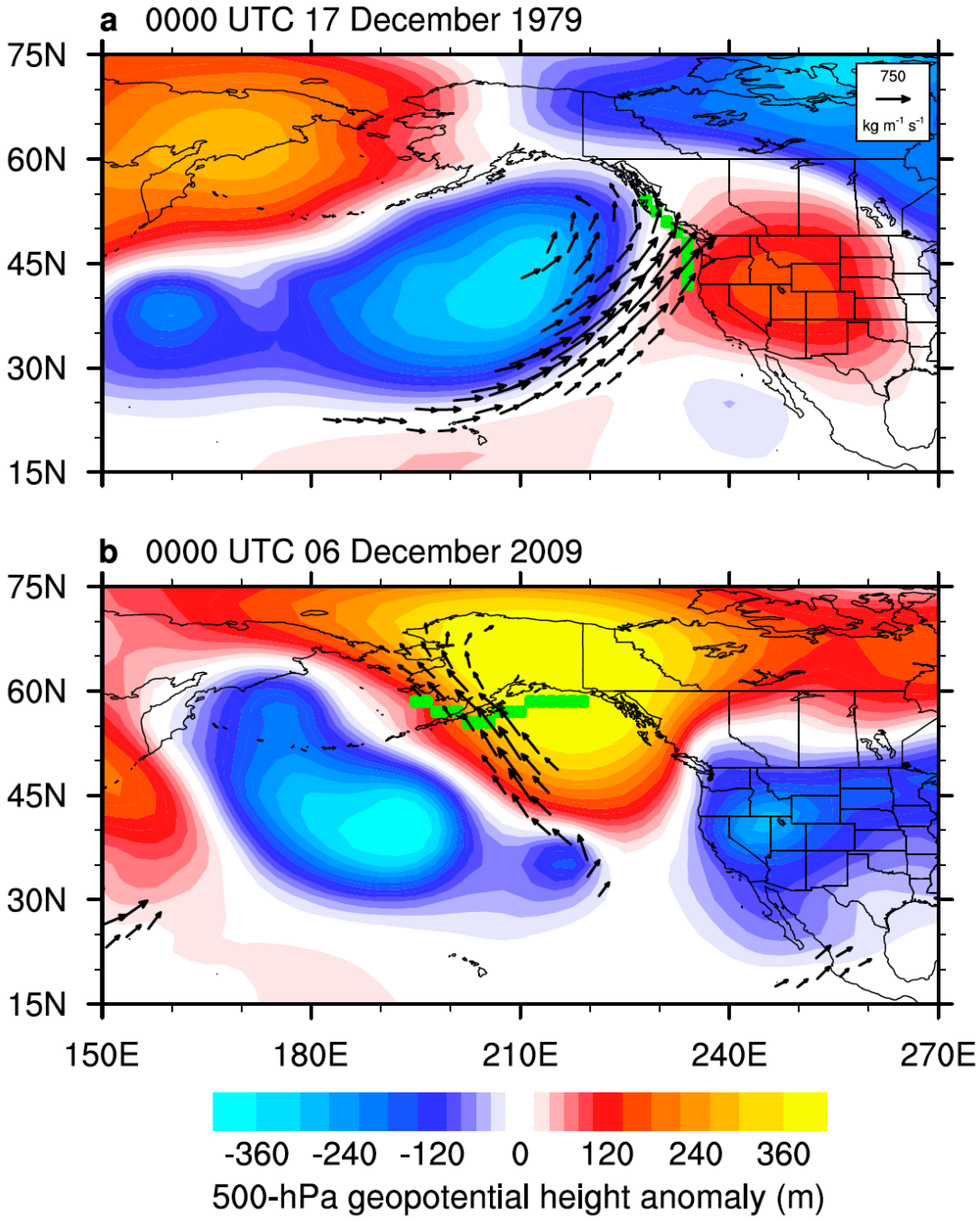
a 0000 UTC 17 December 1979
b 0000 UTC 06 December 2009
75N
60N
45N
30N
15N
150E
180E
210E
240E
270E
750
kg m-1 s-1
-360 -240 -120 0 120 240 360
500-hPa geopotential height anomaly (m)

362

363 **Figure 1.** AR strike events during the third week following phase 5 of the MJO are shown for an
364 AR strike on (**a**) the Pacific Northwest at 0000 UTC 17 December 1979 during an easterly QBO
365 period and (**b**) Alaska at 0000 UTC 06 December 2009 during a westerly QBO period. Black
366 vectors depict IVT_{AR} (kg m^{-1} s^{-1}). A reference vector is located in the upper right corner of (**a**).
367 Shading depicts 500-hPa geopotential height anomalies. The grid points in green specify the
368 particular grid points used to identify ARs that strike (**a**) the Pacific Northwest and (**b**) Alaska
369 throughout the text. The figure derives from ERA-Interim data [*Dee et al.*, 2011].

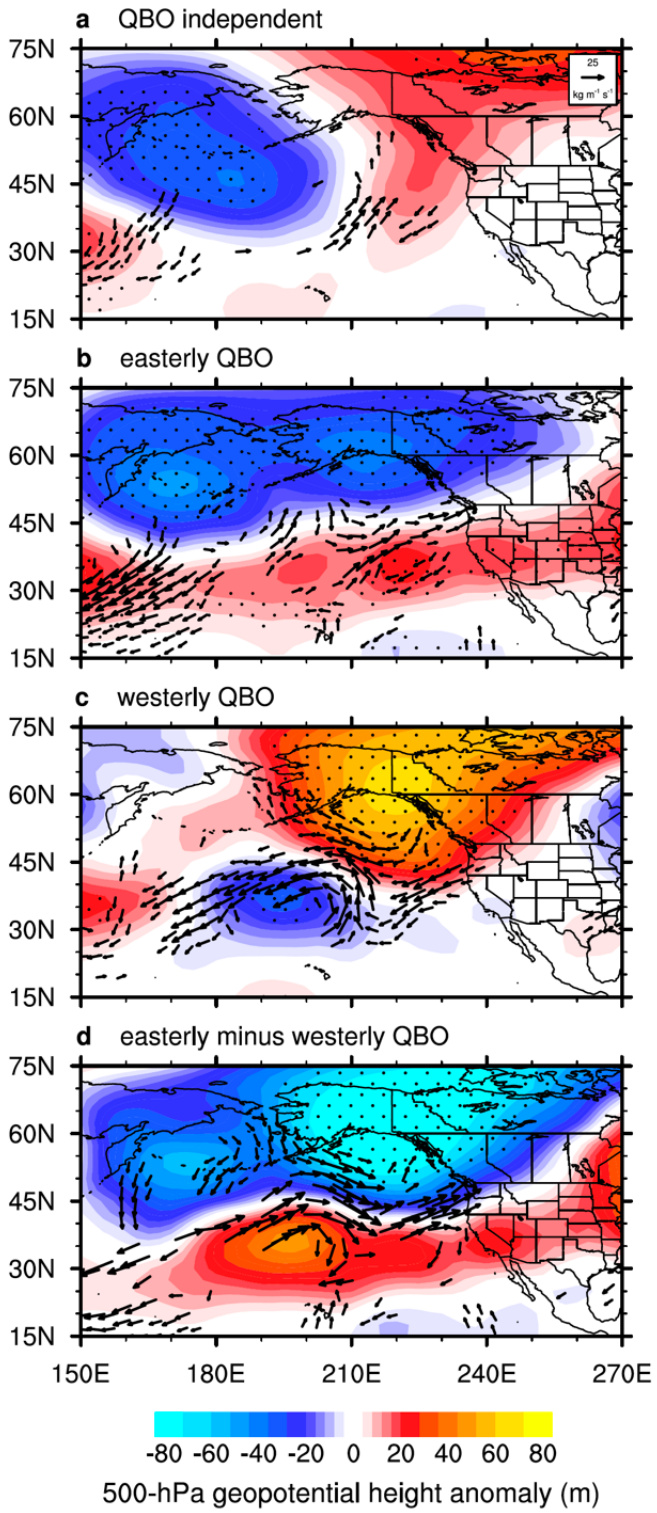
a QBO independent
b easterly QBO
c westerly QBO
d easterly minus westerly QBO
75N
60N
45N
30N
15N
150E
180E
210E
240E
270E
25
kg m-1 s-1
-80 -60 -40 -20 0 20 40 60 80
500-hPa geopotential height anomaly (m)

370

371 **Figure 2.** Observational composites averaged over the third week following days when the MJO
372 was in phase 5 are shown for days (**a**) independent of the phase of the QBO, (**b**) during easterly
373 QBO periods, (**c**) during westerly QBO periods, and (**d**) the easterly QBO composite minus the
374 westerly QBO composite. Only days during November-February are composited. Black vectors
375 depict anomalous IVT_{AR} (kg m^{-1} s^{-1}), with only those vectors with magnitudes $\geq$ 10 kg m^{-1} s^{-1}
376 and with either component statistically significant at the 2% level plotted. A reference vector is
377 located in the upper right corner of (**a**). Two iterations of nine-point local smoothing were
378 applied to the components of the vectors before plotting. Shading depicts 500-hPa geopotential
379 height anomalies, with its statistical significance at the 2% level indicated by stippling, as
380 determined by a Monte Carlo simulation (Text S11). Sample sizes are provided in Table S1. The
381 figure derives from ERA-Interim data [*Dee et al.*, 2011].

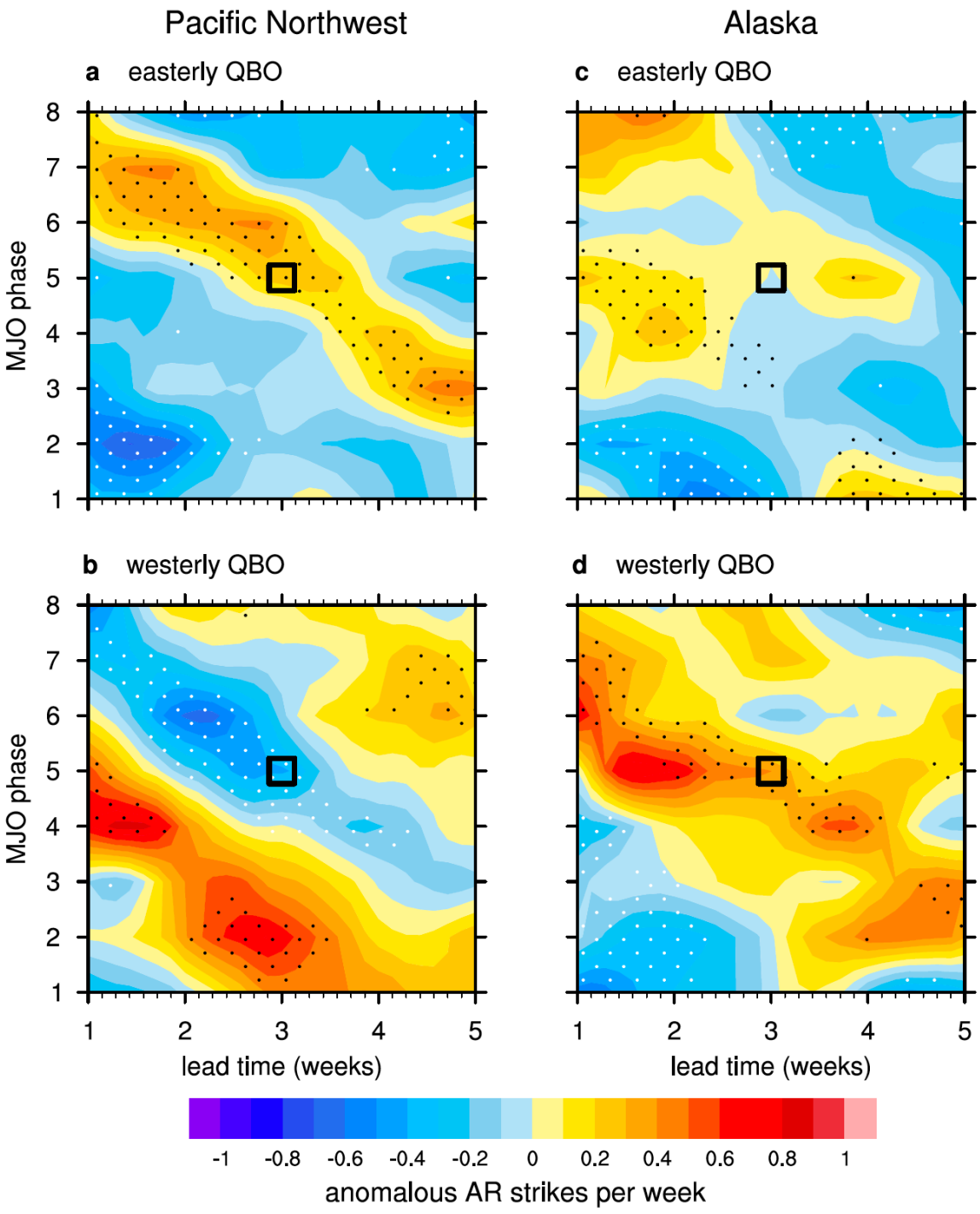
Pacific Northwest
Alaska
a easterly QBO
c easterly QBO
b westerly QBO
d westerly QBO
MJO phase
lead time (weeks)
anomalous AR strikes per week
-1
-0.8
-0.6
-0.4
-0.2
0
0.2
0.4
0.6
0.8
1

382

Figure 3. Observational composites are shown of anomalous AR strikes per week following days when the MJO was in a particular phase for (**a)** the Pacific Northwest and (**c**) Alaska during easterly QBO periods and for (**b**) the Pacific Northwest and (**d**) Alaska during westerly QBO periods. Only days during November-February are composited. The detection grid points for the Pacific Northwest and Alaska are specified in Figures 1a and 1b, respectively. The ordinate indicates the MJO phase of the days being composited; the abscissa indicates the lead time (weeks) that passes between the occurrence of a particular MJO phase and the anomalous AR strikes during that week. For example, the black square highlights the anomalous AR strikes during the third week (days 15 to 21) following days when the MJO was in phase 5. To demonstrate robustness, each panel has its grid points ranked according to the percentage of individual anomalous AR strikes per week values that are positive within the composite. Black stippling is overlaid on the top 20% of these ranked grid points; white stippling is overlaid on the bottom 20%. Sample sizes are provided in Table S1. The figure derives from ERA-Interim data [*Dee et al.*, 2011].

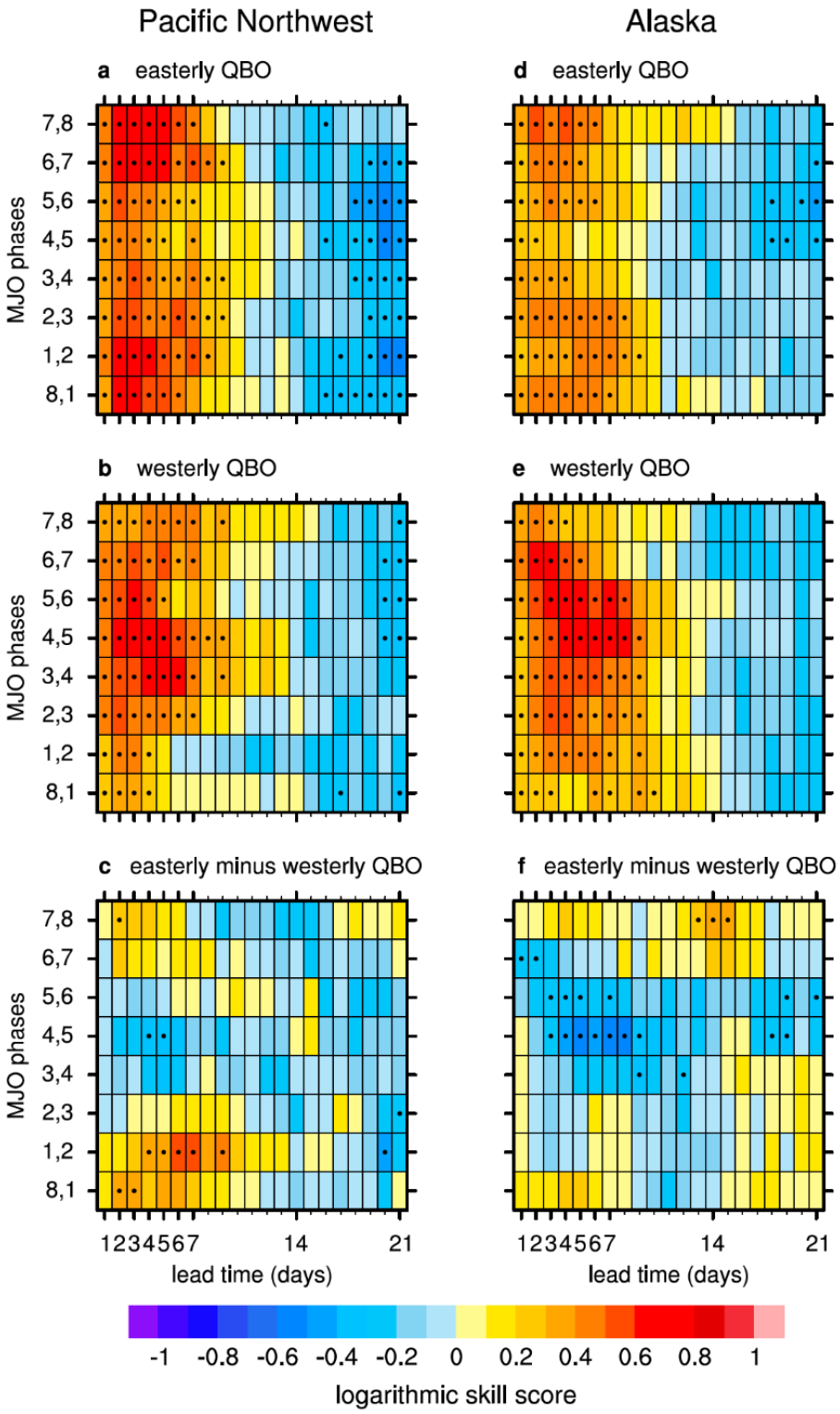
Pacific Northwest
Alaska
a easterly QBO
d easterly QBO
b westerly QBO
e westerly QBO
c easterly minus westerly QBO
f easterly minus westerly QBO
MJO phases
7,8
6,7
5,6
4,5
3,4
2,3
1,2
8,1
1234567
14
21
lead time (days)
-1
-0.8
-0.6
-0.4
-0.2
0
0.2
0.4
0.6
0.8
1
logarithmic skill score

397

Figure 4. Logarithmic skill scores of the ECMWF reforecast ensemble system are shown for (**a** to **c**) the Pacific Northwest and (**d** to **f**) Alaska, for (**a**) and (**d**) during easterly QBO periods, for (**b**) and (**e**) during westerly QBO periods, and for (**c**) and (**f**) the easterly minus the westerly QBO periods. Only the LSSs of reforecasts that initialized during November-February are calculated. The ordinate indicates the MJO phases (paired to increase sample sizes) of the initialization dates of the reforecasts; the abscissa indicates the lead time (days) that passes between the occurrence of a particular MJO phase and the final day of the forecast period (Text S8). In (**a**), (**b**), (**d**), and (**e**) positive values signify the model has more skill than a climatological reference forecast. Dots indicate their difference is statistically significant at the 5% level. In (**c**) and (**f**) positive values signify that the model has more skill during the easterly QBO than the westerly QBO. Dots indicate their difference is statistically significant at the 5% level. Statistical significance is determined by a two-sided student's t-test. Sample sizes are provided in Table S2. The figure derives from ERA-Interim data [*Dee et al.*, 2011] and ECMWF reforecast ensemble system data [*Vitart et al.*, 2017].